

Antiferromagnetic Order Breaks Inversion Symmetry in a Metallic Double Perovskite, $\text{Pb}_2\text{NiOsO}_6$

Hai L. Feng,^{††} Chang-Jong Kang,^{††} Pascal Manuel, Fabio Orlandi, Yu Su, Jie Chen, Yoshihiro Tsujimoto, Joke Hadermann, Gabriel Kotliar, Kazunari Yamaura, Emma E. McCabe,* and Martha Greenblatt*



Cite This: *Chem. Mater.* 2021, 33, 4188–4195



Read Online

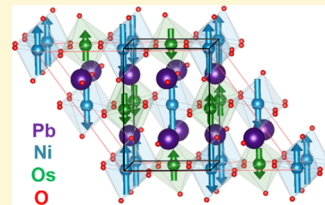
ACCESS |

Metrics & More

Article Recommendations

Supporting Information

ABSTRACT: A polycrystalline sample of $\text{Pb}_2\text{NiOsO}_6$ was synthesized under high-pressure (6 GPa) and high-temperature (1575 K) conditions. $\text{Pb}_2\text{NiOsO}_6$ crystallizes in a monoclinic double perovskite structure with a centrosymmetric space group $P2_1/n$ at room temperature. $\text{Pb}_2\text{NiOsO}_6$ is metallic down to 2 K and shows a single antiferromagnetic (AFM) transition at $T_N = 58$ K. $\text{Pb}_2\text{NiOsO}_6$ is a new example of a metallic and AFM oxide with three-dimensional connectivity. Neutron powder diffraction and first-principles calculation studies indicate that both Ni and Os moments are ordered below T_N and the AFM magnetic order breaks inversion symmetry. This loss of inversion symmetry driven by AFM order is unusual in metallic systems, and the 3d–5d double-perovskite oxides represent a new class of noncentrosymmetric AFM metallic oxides.



1. INTRODUCTION

Transition-metal oxides (TMOs) exhibit unique correlations between magnetism and electrical conductivity: ferromagnetism (FM) in TMOs usually coexists with metallic conductivity, whereas insulating TMOs usually exhibit antiferromagnetism (AFM).¹ Exceptions from this behavior, such as FM insulating oxides and AFM metallic oxides, are less common. CaCrO_3 and Nb_2O_{29} are examples of AFM metallic oxides with three-dimensional crystal structures.^{2–4} Other AFM metallic oxides such as $\text{La}_{2-2x}\text{Sr}_{1+2x}\text{Mn}_2\text{O}_7$ and $\text{Ca}_3\text{Ru}_2\text{O}_7$ crystallize in layered crystal structures, and FM couplings are dominant within the layer.^{5,6} Recently, RuO_2 , and LaNiO_3 , which had been described as paramagnetic metals, were found to be AFM-ordered and are new examples of AFM metallic oxides with three-dimensional crystal and electronic structures.^{7–9}

5d TMOs are unique correlated systems because of the spatial extent of the 5d electrons, generally giving 5d TMOs wider bandwidths (W), stronger spin–orbit coupling (SOC), and smaller on-site Coulomb repulsion (U) compared with 3d TMOs.¹⁰ For instance, metal–insulator transitions driven by AFM orders were proposed in 5d oxides, $\text{Pb}_2\text{CaOsO}_6$,¹¹ $\text{Cd}_2\text{Os}_2\text{O}_7$,^{12,13} and NaOsO_3 ,¹⁴ and a ferroelectric-like structural-transition-breaking inversion symmetry has been observed in metallic LiOsO_3 .¹⁵ Recent studies on a 5d metallic oxide $\text{Pb}_2\text{CoOsO}_6$ demonstrated that the AFM order breaks inversion symmetry.^{16,17} In this work, we have built on this, synthesizing a new 5d hybrid double perovskite oxide $\text{Pb}_2\text{NiOsO}_6$, which is a new example of an AFM metallic oxide. Characterization using neutron powder diffraction (NPD) and property measurements suggest that the magnetic order breaks inversion symmetry (similar to reports on $\text{Pb}_2\text{CoOsO}_6$).¹⁶ First-principles calculations confirm that both Ni and Os moments are ordered, allowing us to confirm

the nature of the ground state (which has not been fully explored previously). The 3d–5d double-perovskite oxides establish a new class of noncentrosymmetric AFM metallic oxides, and our symmetry analysis of $\text{Pb}_2\text{NiOsO}_6$ explores how this understanding can be applied more widely to design new magnetoelectrics.

2. EXPERIMENTAL SECTION

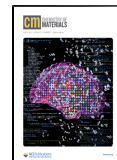
Polycrystalline $\text{Pb}_2\text{NiOsO}_6$ was synthesized via a solid-state reaction from powders of PbO_2 (99%, Alfa), Os (99.95%, Heraeus Materials), NiO (99.997%, Alfa), and KClO_4 (99.99%, Alfa). The powders were thoroughly mixed in a stoichiometric ratio in an Ar-filled glovebox, followed by sealing in a Pt capsule. The Pt capsule was statically and isotropically compressed in a belt-type high-pressure apparatus (Kobe Steel, Ltd., Japan¹⁸), and a pressure of 6 GPa was applied while the capsule was heated at 1400 °C for 1 h, followed by quenching to room temperature in less than a minute. The pressure was then gradually released over several hours.

A dense and black polycrystalline pellet was obtained, and several pieces were cut out from it. A selected piece was finely ground for a synchrotron X-ray diffraction (SXRD) study, which was conducted in a large Debye–Scherrer camera in the BL15XU beamline, SPring-8, Japan.^{19,20} The SXRD pattern was collected at room temperature, and the wavelength was confirmed to be 0.65298 Å by measurement of a standard material, CeO_2 . The absorption coefficient was measured in the same line. The SXRD data were analyzed by the Rietveld method with the RIETAN-VENUS software.²¹ The crystal structure was depicted by VESTA.²²

Received: March 24, 2021

Revised: May 6, 2021

Published: May 26, 2021



The electrical resistivity (ρ) of a polycrystalline pellet of $\text{Pb}_2\text{NiOsO}_6$ was measured by a four-point method at a gauge current of 0.1 mA in a physical property measurement system (PPMS, Quantum Design, Inc.). Electrical contacts were made with Pt wires and Ag paste in the longitudinal direction. The temperature dependence of the specific heat capacity (C_p) was measured in the same PPMS by a thermal relaxation method at temperatures between 2 and 300 K with Apiezon N grease thermally connecting the material to the holder stage.

The magnetic susceptibility (χ) of $\text{Pb}_2\text{NiOsO}_6$ powder was measured in a magnetic property measurement system (Quantum Design, Inc.). The measurement was conducted in field-cooled (FC) and zero-FC conditions in the temperature range between 2 and 390 K. The applied magnetic field was 10 kOe.

Time-of-flight NPD data were collected at the WISH diffractometer (target station 2) at the ISIS Neutron and Muon Source.²³ For the NPD data collection, 3.26 g of $\text{Pb}_2\text{NiOsO}_6$ powder was placed in a 6 mm diameter cylindrical vanadium can under helium and sealed using indium wire. The sample was loaded into a helium cryostat and cooled to base temperature (1.5 K). A high-quality data set was collected at 1.5 K (~1 h, ~40 μA h), and shorter scans (~15 min, ~10 μA h) were collected every 2.5 K on warming to 100 K. A final higher-quality scan (~1 h, ~40 μA h) was collected at 98 K in the paramagnetic phase. Data were analyzed and Rietveld refinements carried out using TopasAcademic,^{24,25} and the web-based ISO-DISTORT software²⁶ was used for symmetry analysis. Rietveld refinements for the antiferromagnetic system were carried out with a nuclear phase and a magnetic-only phase, with atomic displacement parameters (ADPs) for the magnetic sites constrained to be equal to those sites in the nuclear phase. A separate peak shape was refined for the magnetic-only phase.

The density functional theory (DFT) calculation was performed on $\text{Pb}_2\text{NiOsO}_6$ with the all-electron full-potential linearized augmented plane-wave method implemented in the WIEN2k code.²⁷ Generalized gradient approximation (GGA) of Perdew–Burke–Ernzerhof (PBE)²⁸ was used for the exchange–correlation functional. The SOC was taken into account in the second variation method. To consider the correlation effect, GGA + U was adopted within fully localized limits.^{29,30} The on-site Coulombic interaction parameters $U = 4$ and 2 eV for Ni and Os, respectively, and the Hund's coupling $J_{\text{H}} = 0.8$ eV, which was shown to describe a similar compound, $\text{Ca}_2\text{NiOsO}_6$ properly.³¹

3. RESULTS

3.1. Crystal Structure. Room-temperature SPXD data of $\text{Pb}_2\text{NiOsO}_6$ were successfully fitted by a monoclinic double perovskite structure with space group $P2_1/n$ (see Supporting Information) similar to that reported for $\text{Pb}_2\text{CoOsO}_6$,¹⁸ $\text{Pb}_2\text{MnReO}_6$,³² and $\text{Pb}_2\text{CoTeO}_6$.³³ Due to the weak X-ray scattering power of O (especially in the presence of strong scatterers Os and Pb), complementary NPD data were used to confirm this nuclear structure at 98 K. NPD data collected at 98 K (above T_N) are consistent with the SPXD results and can be well fitted with a model of $P2_1/n$ symmetry (see the Supporting Information). The Ni and Os ions occupy $2a$ and $2b$ sites, respectively. Allowing for antisite disorder in the model during the refinement (with constraints to maintain stoichiometry) revealed complete B -site ordering (100(6)%). Refinement of the occupancies of Pb and O sites (with a single global ADP) indicated that the material is very close to stoichiometric ($\text{Pb}_{1.940(1)}\text{NiOsO}_{5.90(1)}$). This stoichiometry was assumed for further analysis. Trace amounts of PbO_2 and NiO impurities were identified and included in the refinement (no Os impurity was detected). Final refined atomic parameters and selected bond lengths and angles are summarized in the Supporting Information. The bond valence sum calculations^{34,35} support the nominal Ni^{2+} and Os^{6+} oxidation states

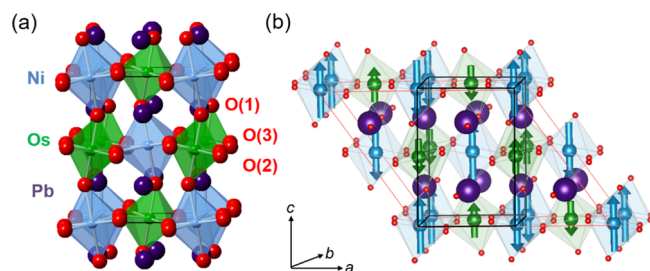


Figure 1. Illustration of the nuclear (a) and magnetic structures (b) of $\text{Pb}_2\text{NiOsO}_6$ at 1.5 K from Rietveld refinement using NPD data; Pb, Ni, Os, and O sites are shown in purple, blue, green, and red, respectively; Ni and Os moments are shown by arrows. The nuclear unit cell is shown by solid black lines and the larger, monoclinic P_{a} magnetic unit cell by solid red lines.

(see the Supporting Information). The refined crystal structure is shown in Figure 1a, where the corner-linked NiO_6 and OsO_6 octahedra are ordered in the rock salt manner. The interoctahedral Ni–O–Os bond angles are 159.20(9), 161.3(4), and 160.5(4)°, which significantly deviate from 180° and imply substantial rotations of BO_6 octahedra.

3.2. Electrical and Magnetic Properties. The temperature dependence of resistivity (ρ) data decreases with cooling, as shown in Figure 2a, and shows the metallic nature of $\text{Pb}_2\text{NiOsO}_6$. The temperature dependence of magnetic susceptibility (χ) data shows a typical AFM transition with a peak at 58 K (see Figure 2b), which indicates the Néel temperature (T_N). The long-range AFM transition was further

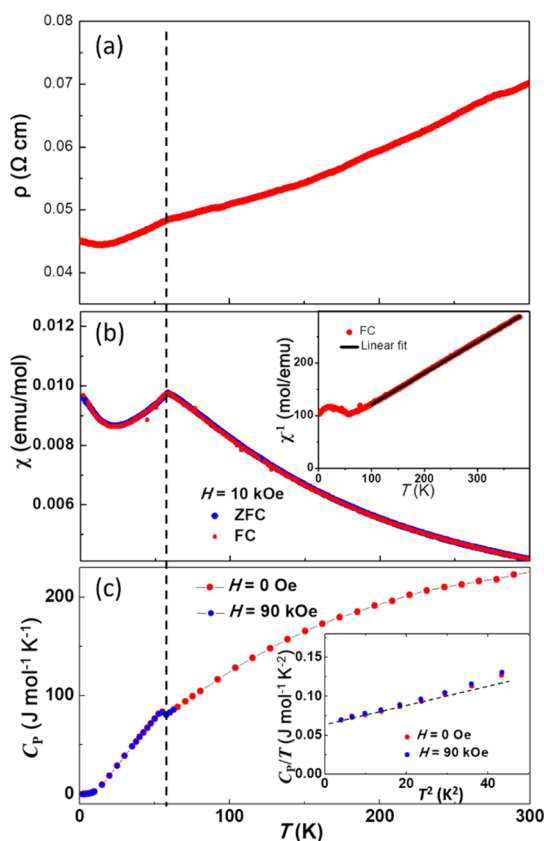


Figure 2. (a) Temperature-dependent resistivity, (b) temperature-dependent magnetic susceptibility, and (c) temperature-dependent specific heat of $\text{Pb}_2\text{NiOsO}_6$.

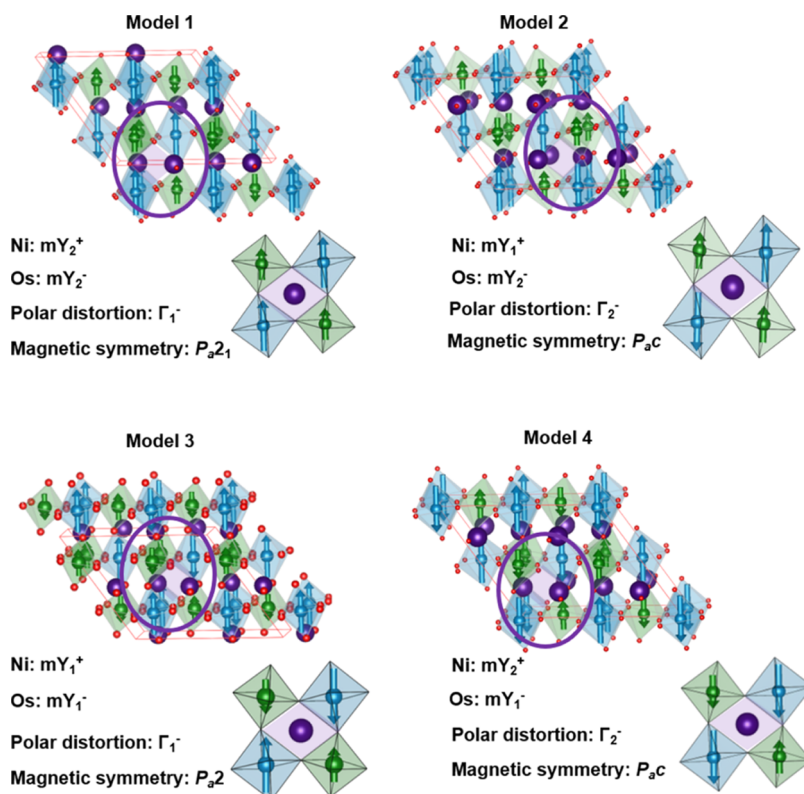


Figure 3. Four magnetic structures that result from the $k = (1/2 \ 0 \ 1/2)$ magnetic propagation vector for the $P2_1/n$ nuclear structure for $\text{Pb}_2\text{NiOsO}_6$ with a magnetic order on both Ni (blue) and Os (green) sites. To help visualize the difference between the four magnetic structures, the magnetic order around a PbO_{12} site (purple) viewed down the $[-1 \ 1 \ 0]$ direction of the nuclear unit cell is highlighted for each model. (Note that for model 2, the magnetic order around the PbO_{12} site is viewed along $[0 \ -1 \ 0]$ of the magnetic unit cell to show the magnetic moments about the same point in the nuclear structure).

confirmed by specific heat data which display a λ -type anomaly at T_N (see Figure 2c). The χ^{-1} versus T data above the T_N show the Curie–Weiss behavior. Fitting the CW law to the data between 100 and 380 K results in an effective moment (μ_{eff}) of $3.66 \ \mu_{\text{B}}$ per formula unit (f.u.) and a Weiss temperature (θ_W) of -102 K . The obtained effective moment is comparable to that in other Ni^{2+} – Os^{6+} double perovskites, $3.44 \ \mu_{\text{B}}/\text{f.u.}$ for $\text{Sr}_2\text{NiOsO}_6$ ³⁶ and $3.46 \ \mu_{\text{B}}/\text{f.u.}$ for $\text{Ba}_2\text{NiOsO}_6$.³⁷ These values are smaller than the spin-only moments of $4.0 \ \mu_{\text{B}}$ per formula unit for the Ni^{2+} ($3d^8$: $S = 1$) and Os^{6+} ($5d^2$: $S = 1$), which may be due to the SOC of Os^{6+} . The negative θ_W corroborates that AFM interactions are dominant in $\text{Pb}_2\text{NiOsO}_6$, which is consistent with the AFM order. The low-temperature part of specific heat data is plotted in the C_p/T versus T^2 , and the lowest temperature part can be characterized by an approximated Debye model ($C_p/T = \gamma + \beta_0 T^2$). The fitting gives a Sommerfeld coefficient (γ) of $63.5 \text{ mJ mol}^{-1} \text{ K}^{-2}$. The large γ value is consistent with the metallic nature of $\text{Pb}_2\text{NiOsO}_6$. The deviation from linearity above 30 K^2 could be due to the lattice contribution.

3.3. Magnetic Structure. To study the magnetic structure of $\text{Pb}_2\text{NiOsO}_6$, NPD data were collected from 1.5 to 98 K. On cooling below 57 K, additional reflections were observed in NPD patterns, which increased smoothly in intensity on cooling (see the Supporting Information). These were consistent with magnetic ordering described by magnetic propagation vector $k = (1/2 \ 0 \ 1/2)$. As described for the double perovskites $\text{Pb}_2\text{CoOsO}_6$ ¹⁶ and for the k_1 propagation vector for $\text{Sc}_2\text{NiMnO}_6$,³⁸ there are four irreps associated with the magnetic propagation vector $k = (1/2 \ 0 \ 1/2)$: mY_1^\pm and

mY_2^\pm . The mY_1^+ (mY_1^-) irreps describe magnetic order on the Ni (Os) sites only. Magnetic susceptibility and heat capacity measurements for $\text{Pb}_2\text{NiOsO}_6$ (Figure 2b,c) and the evolution of magnetic Bragg intensity in NPD data collected on cooling (see the Supporting Information) suggest a single magnetic ordering transition which could result from one of three possible scenarios: (1) only Ni^{2+} moments order at T_N ; (2) only Os^{6+} moments order at T_N or (3), both Ni^{2+} and Os^{6+} moments order simultaneously at T_N . As described for related double perovskites,^{36,38–40} the magnetic moments on the two B sites are strongly correlated in refinements and NPD cannot unambiguously distinguish between these three scenarios. However, given the strong coupling between nearest Ni^{2+} and Os^{6+} ions in $\text{Ca}_2\text{NiOsO}_6$, it seems most likely that both Ni and Os sublattices order magnetically below T_N .³¹ Experiments on $\text{Pb}_2\text{CoOsO}_6$ including muon spin rotation experiments support magnetic ordering of both Co^{2+} and Os^{6+} moments,¹⁶ consistent with our analysis for $\text{Pb}_2\text{NiOsO}_6$. Mode inclusion analysis^{41,42} using 1.5 K data suggested that the greatest improvement in fit was obtained with moments on the Os sites described by mY_2^- (R_{wp} decreased from 7.71% for a nonmagnetic model to 6.42% for the mY_2^- model) with Os moments close to the $[0 \ 0 \ 1]$ direction of the $P2_1/n$ nuclear unit cell. Magnetic ordering described by the mY_2^- irrep on the Os sites and the mY_1^+ (mY_2^+) irrep on the Ni sites breaks inversion symmetry, and the ferroelectric mode Γ_2^- (Γ_1^-) is coupled to both magnetic order parameters, allowing polar displacements in the ac plane ($[0 \ 1 \ 0]$ direction) of the $P2_1/n$ nuclear unit cell. These two possible structures are very similar, and our NPD data do not allow us to confirm which is more

appropriate to describe the low-temperature nuclear and magnetic structure of $\text{Pb}_2\text{NiOsO}_6$. Attempts to investigate the polar distortions using both NPD analysis and electron diffraction were not successful, suggesting that these distortions are very subtle. Consistent with DFT calculations (see below), the $mY_2^- mY_1^+ \Gamma_2^-$ model was assumed for all further analysis. This magnetic structure is described by the monoclinic unit cell of symmetry $P_a\bar{c}$ which is related to the $P2_1/n$ nuclear unit cell by the basis vectors $(-2\ 0\ 0)$ $(0\ -1\ 0)$ $(1\ 0\ 1)$ with an origin shift of $(0\ 1/4\ 0)$ (see Figure 1b). Given the complexity of the system, the moments on Ni and Os sites were constrained to be collinear (as observed in related systems^{16,31,34,38–40,43}) and the moments on Os sites were constrained to be eight times smaller than those on Ni sites, as might be expected for Ni^{2+} (d^8) and Os^{6+} (d^2) with significant covalent bonding.^{16,31,36,39} Allowing the moment direction to refine freely gave moments close to $[0\ 0\ 1]$ of the $P2_1/n$ nuclear unit cell, and constraining the moments to lie exactly along this direction gave a similar fit (R_{wp} was the same to three decimal places) and was used in subsequent analysis. Allowing ADPs to refine anisotropically did not give a significant improvement in fit and ADPs were found to be fairly isotropic. The final refinement profiles and parameters are given in the Supporting Information.

Sequential Rietveld refinements were carried out using NPD data collected on warming to study the evolution of nuclear and magnetic structures. The 1.5 K model described above was used, and this sequential analysis suggested a fairly smooth expansion of the structure on warming (see the Supporting Information).

3.4. First-Principles Calculations. DFT calculations were carried out to explore whether both Ni and Os moments are ordered in the magnetic phase of $\text{Pb}_2\text{NiOsO}_6$ and to differentiate between the possible magnetically ordered structures. First, the total energies were calculated for magnetic models with either AFM order on both Ni and Os sublattices or AFM order only on the Ni sublattice (see the Supporting Information). These calculations indicate that the model with the AFM order on both Ni and Os sublattices is 0.102 eV per formula unit more stable than that with only Ni-ordered moments. These calculations support the noncentrosymmetric AFM models in which both sublattices are ordered.

As discussed above, group theory calculations assuming the propagation vector $(1/2\ 0\ 1/2)$ and magnetic order on both Ni and Os sublattices (from magnetic irreps mY_1^+ and mY_2^+ on Ni sites, mY_1^- and mY_2^- on Os sites) give four possible isotropy subgroups (Figure 3). These models give comparable fits to the NPD data, and we are not able to unambiguously determine the magnetic ground state from our experimental work. Although the relative orientation of magnetic spins is similar in these four structures (they all have the $\uparrow\downarrow\downarrow\uparrow\uparrow$ sequence of moments on the Ni–Os chains along the $[0\ 0\ 1]$ direction of the nuclear unit cell), the superposition of the magnetic order on the nuclear structure (with monoclinic symmetry arising from rotations of NiO_6 and OsO_6 octahedra) results in different final symmetries and, as a consequence, in different distortions (e.g., polar degrees of freedom, bond distances, and angles) and hence different macroscopic properties.^{44–46} Since the four models derive from different combinations of irreducible representations, these are distinct structures and not translational domains.

DFT calculations were carried out to differentiate between these similar magnetic structures and to determine the ground

state. Calculations were carried out using the GGA(PBE) + SOC + U scheme to determine the energy of the four magnetic structures shown in Figure 3, and the relative energies are given in Table 1. Model 2 (described above from analysis of

Table 1. Total Energy and Magnetic Moment Calculated for $\text{Pb}_2\text{NiOsO}_6$ for Models Shown in Figure 3^a

	energy (meV/atom)	total moment (μ_B)	spin moment (μ_B)	orbital moment (μ_B)
model 1	0	Ni: 1.85	Ni: 1.70	Ni: 0.15
		Os: 0.78	Os: 0.99	Os: -0.21
model 2	-0.36	Ni: 1.86	Ni: 1.70	Ni: 0.16
		Os: 0.78	Os: 0.99	Os: -0.21
model 3	+0.18	Ni: 1.85	Ni: 1.70	Ni: 0.15
		Os: 0.77	Os: 0.99	Os: -0.22
model 4	+0.42	Ni: 1.85	Ni: 1.70	Ni: 0.15
		Os: 0.76	Os: 0.99	Os: -0.23

^aUnit of the energy is meV per atom and is calculated by dividing the DFT total energy by the number of atoms in the unit cell (40 for the magnetic unit cells shown in Figure 3). Model 1 is chosen as the reference energy. Details about magnetic moments are discussed in the main text.

NPD data, Figure 1b) is found to be the lowest in energy for calculations including SOC (Table 1). These results suggest that the ground state of $\text{Pb}_2\text{NiOsO}_6$ is best described by $P_a\bar{c}$ magnetic symmetry, with Γ_2^- polar degrees of freedom, consistent with the ground state reported for $\text{Pb}_2\text{CoOsO}_6$.¹⁶ Notice that the same ground state was also found for $\text{Pb}_2\text{NiOsO}_6$ from calculations without accounting for SOC. Mode decomposition of the relaxed structures from these DFT calculations was carried out using ISODISTORT,²⁶ but the amplitudes of polar displacements were very small (≤ 0.00035); this is consistent with NPD and electron diffraction analysis, both unable to confirm these displacements. The subtlety of these polar distortions (and that they are secondary rather than primary order parameters) is borne out by the fact that the two lowest energy structures (models 1 and 2) allow different polar distortions, suggesting that these distortions play a minor role in giving the noncentrosymmetric ground-state structure.

The electronic structure of $\text{Pb}_2\text{NiOsO}_6$ for model 2 (total and partial) is shown in Figure 4. Since Ni and Os atoms have local magnetic moments (Table 1), they show local spin polarization, as shown in Figure 4b,c. These local spin polarizations are summed to be zero, that is, the net total magnetic moment is zero, reflecting that $\text{Pb}_2\text{NiOsO}_6$ is antiferromagnetic, as demonstrated in Figure 4a.

The major contributions to the total DOS around the E_F are attributed to the Os 5d orbitals in both spin channels, which hybridize strongly with the O 2p orbitals. Occupation numbers for Ni 3d and Os 5d are 7.81 and 3.80, respectively. The huge hybridization indicated between Os 5d and O 2p orbitals suggests Ni^{2+} and Os^{6+} formal oxidation states in $\text{Pb}_2\text{NiOsO}_6$, consistent with the magnetic susceptibility experiment. Spin and orbital moments for Ni are 1.70 and 0.16 μ_B , respectively, thereby giving a total magnetic moment of 1.86 μ_B per Ni. For Os, spin and orbital moments are 0.99 and -0.21 μ_B , respectively, where the minus sign indicates that the orbital moment is opposite the spin direction; thus, the total moment is 0.78 μ_B per Os. These calculated moments are comparable with those obtained from NPD analysis (see above). The calculated γ is 7.1 $\text{mJ mol}^{-1} \text{K}^{-2}$. This is much smaller than the

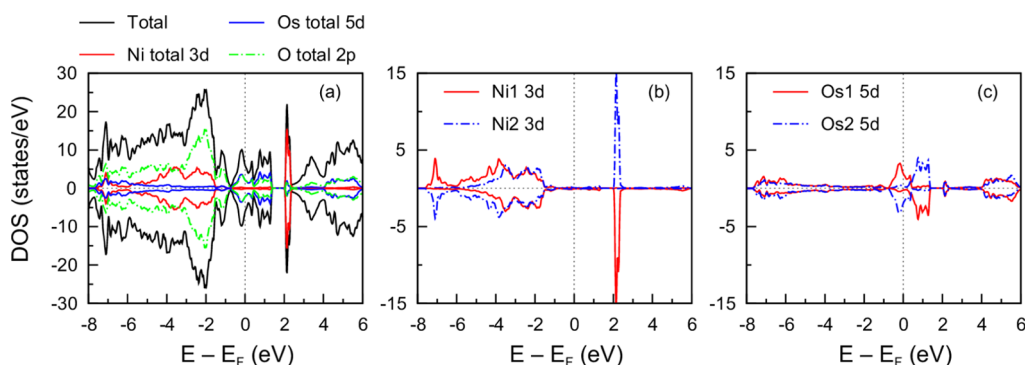


Figure 4. Total and partial density of states (PDOS) of $\text{Pb}_2\text{NiOsO}_6$ for model 2 from GGA + SOC + U calculation. (a) Black solid line corresponds to the total DOS. Red solid, blue solid, and green dashed dotted lines represent total Ni 3d, total Os 5d, and O 2p PDOS, respectively. (b) PDOS for each Ni 3d: Ni1 (Ni2) is presented for the spin majority as spin up (down). (c) PDOS for each Os 5d: Os1 (Os2) is presented for the spin majority as spin up (down). The positive and negative values in DOS correspond to spin up and down, respectively.

one obtained from the fitting of low-temperature specific heat data ($63.5 \text{ mJ mol}^{-1} \text{ K}^{-2}$), which may be due to the fact that DFT underestimates the electronic correlations in the correlated systems, resulting in a relatively small γ value.

4. DISCUSSION

The $A_2\text{NiOsO}_6$ ($A = \text{Ca}^{2+}$, Sr^{2+} , Ba^{2+} , and now Pb^{2+}) oxides adopt B -site ordered double perovskite structures and span a range of properties, from insulating ($A = \text{Ca}$ ³¹) to metallic ($A = \text{Pb}$) and from ferromagnetic ($A = \text{Ba}$ at low temperatures³⁷) to antiferromagnetic ($A = \text{Sr}$ ³⁶). While all these analogues adopt rocksalt ordering of NiO_6 and OsO_6 octahedra, the degree of tilting of these octahedra increases with decreasing A cation radius: $\text{Ba}_2\text{NiOsO}_6$ is cubic with 180° Ni–O–Os bond angles; in tetragonal $\text{Sr}_2\text{NiOsO}_6$, octahedra are tilted around the long axis, giving $180^\circ/166^\circ$ Ni–O–Os angles,³⁶ while $\text{Ca}_2\text{NiOsO}_6$ adopts the monoclinic $P2_1/n$ structure (with $a^-a^-c^+$ tilts) with Ni–O–Os angles of $\sim 151^\circ$.³⁶ $\text{Pb}_2\text{NiOsO}_6$ also adopts this $P2_1/n$ structure despite the ionic radius of Pb^{2+} (1.49 Å) being comparable to that of Sr^{2+} (1.44 Å);⁴⁷ this might in part be due to the inert pair Pb^{2+} ion favoring the lower-symmetry coordination environment⁴⁸ possible in the $P2_1/n$ structure: Pb occupies the $4e$ site of 1 symmetry in $P2_1/n$ compared with the higher-symmetry $4d$ site of $\bar{4}$ symmetry in the $I4/m$ structure of $\text{Sr}_2\text{NiOsO}_6$.

The magnetic structure described here for $\text{Pb}_2\text{NiOsO}_6$ is of the same symmetry as that reported for $\text{Pb}_2\text{CoOsO}_6$,¹⁶ although with a slightly different orientation of moments, likely resulting from the different magnetic anisotropies of Co^{2+} and Ni^{2+} ions in octahedral coordination environments. In both $\text{Pb}_2\text{NiOsO}_6$ and $\text{Pb}_2\text{CoOsO}_6$, the magnetic order on the Ni/Co and Os sublattices breaks inversion symmetry and follows an $\uparrow\downarrow\downarrow$ sequence along $[0\ 0\ 1]$ of the nuclear unit cell. Magnetic ordering has been shown to break inversion symmetry in other perovskites, including $\text{Sr}_2\text{NiMnO}_6$, but with weak coupling between Ni and Mn sublattices,³⁸ in contrast to Pb_2BOSO_6 ($B = \text{Co, Ni}$), which seem to have collinear moments on both B and Os sublattices and a single magnetic ordering transition. These observations are consistent with strong couplings between Co/Ni and Os sublattices. This $\uparrow\downarrow\downarrow$ magnetic structure observed in $\text{Pb}_2\text{NiOsO}_6$ is significantly different from those reported for other $A_2\text{NiOsO}_6$ double perovskites. Previous works have highlighted the importance of both nearest-neighbor (likely FM) and next-nearest-neighbor (likely AFM) interactions in these sys-

tems.^{31,49} The balance between these (competing) interactions gives some magnetic frustration in $\text{Sr}_2\text{NiOsO}_6$ and makes the magnetic structure of $A_2\text{NiOsO}_6$ phases very sensitive to bond angles.³¹

The symmetry requirements for magnetic order to break inversion symmetry have been explored by Perez-Mato et al.⁵⁰ and provide a recipe for designing new magnetoelectrics. If the magnetic k vector is not compatible with the screw axes or glide planes of the nuclear (paramagnetic) unit cell (when time reversal symmetry is considered), then full magnetic order on a lattice of magnetic atoms on special sites (of 1 symmetry) will break the inversion symmetry, resulting in noncentrosymmetric structures.

The double perovskites considered here have rocksalt ordering of B and B' cations on sites related by an origin shift (and typically with symmetries including inversion centers). If a single magnetic propagation vector k describes the magnetically ordered phase, and full magnetic order is expected on both B and B' sublattices, then, depending on k , the irreps to describe the magnetic order on each sublattice may be of opposite parity with respect to an inversion center at the origin. These irreps couple to a noncentrosymmetric distortion (Γ_x^-), breaking inversion symmetry. This is the case described here for $\text{Pb}_2\text{NiOsO}_6$ for $k = (1/2\ 0\ 1/2)$ and also for $k = (-1/2\ 1/2\ 1/2)$. Likewise for a cubic double perovskite $A_2\text{BB}'\text{O}_6$ of $Fm\bar{3}m$ nuclear symmetry (with magnetic B and B' ions on $4a$ and $4b$ sites, respectively), a magnetic $k = (1/2\ 1/2\ 1/2)$ would have a similar effect. This is also observed in the hexagonal $\text{Ca}_3\text{CoMnO}_6$ ($R\bar{3}c$ nuclear symmetry, Mn^{3+} and Co^{3+} ions on $6a$ (0 0 1/4) and $6b$ (0 0 0) sites, respectively) with magnetic $k = (0\ 0\ 0)$ giving the well-known $\uparrow\uparrow\downarrow\downarrow$ polar magnetic structure.⁵¹

If suitable cation-ordered structures with strong magnetic coupling between the two sublattices (to favor them ordering with the same magnetic k vector) can be identified, then new magnetoelectrics might be designed if the magnetic exchange interactions can be balanced to give the desired k vector. We note that the improper ferroelectricity described here does not require additional ordering of A -site cations (e.g., the $\text{AA}'\text{NiOsO}_6$ phases explored recently).⁵²

It is striking that both $\text{Pb}_2\text{NiOsO}_6$ and $\text{Pb}_2\text{CoOsO}_6$ ¹⁶ are metallic, in contrast to the SOC Mott-insulating nature of $\text{Ca}_2\text{NiOsO}_6$ and $\text{Ca}_2\text{CoOsO}_6$,³¹ despite the structural similarities between these Pb and Ca analogues. First, we note that although $\text{Pb}_2\text{NiOsO}_6$ is metallic, its resistivity is

several orders of magnitude higher than that of $\text{Pb}_2\text{CoOsO}_6$ (300 K resistivity is $\sim 0.07 \Omega \text{ cm}$ (Figure 2a) and $\sim 3.5 \times 10^{-4} \Omega \text{ cm}$ for Ni and Co¹⁶ analogues, respectively). This is similarly observed for $\text{Ca}_2\text{NiOsO}_6$ and $\text{Ca}_2\text{CoOsO}_6$ and is ascribed to the full occupancy of the Ni^{2+} t_{2g} band reducing delocalization of Os^{6+} t_{2g} electrons.³¹

The half-metallic nature proposed for $\text{Sr}_2\text{NiOsO}_6$ results from the partially-occupied Os t_{2g} states crossing the Fermi level, with SOC broadening the Os 5d bands.⁵³ This scenario can be applied to A_2NiOsO_6 ($\text{A} = \text{Ca, Pb}$), and our PDOS calculations (Figure 4) are qualitatively similar to those reported for $\text{Ca}_2\text{NiOsO}_6$ ³¹ (with Ni t_{2g} states below $\sim -2 \text{ eV}$ and a narrow band of Ni e_g states at $\sim 2 \text{ eV}$, with Os 5d and O 2p bands crossing E_F). However, the bandwidth in these double perovskites is also influenced by Ni–O–Os bond angles: in $\text{Ca}_2\text{NiOsO}_6$ with small Ca^{2+} ions, the Ni–O–Os angles ($\sim 149.3\text{--}150.6^\circ$ at 4 K)³⁶ show much larger deviations from the ideal 180° bond angles than in $\text{Pb}_2\text{NiOsO}_6$ ($158.8\text{--}161.0^\circ$ at 1.5 K). The more distorted structure reported for the Ca analogues is likely to decrease the orbital overlap and bandwidth, giving wider band gaps than the less distorted Pb analogues. This is consistent with the insulating and more localized nature of $\text{Ca}_2\text{NiOsO}_6$ and its higher magnetic ordering temperature (158 K, compared with $T_N = 58 \text{ K}$ for $\text{Pb}_2\text{NiOsO}_6$).

5. CONCLUSIONS

A new 5d oxide $\text{Pb}_2\text{NiOsO}_6$ was synthesized under high pressure. $\text{Pb}_2\text{NiOsO}_6$ crystallizes in a monoclinic double perovskite structure with a centrosymmetric space group $P2_1/n$ at room temperature. $\text{Pb}_2\text{NiOsO}_6$ is metallic down to 2 K and displays an AFM transition with $T_N = 58 \text{ K}$. $\text{Pb}_2\text{NiOsO}_6$ is a new example of AFM metallic oxides with three-dimensional crystal and electronic structures. NPD and DFT calculations indicate that both the Ni and Os moments are ordered below T_N , breaking inversion symmetry, which is similar to recently reported $\text{Pb}_2\text{CoOsO}_6$.^{16,17} The magnetically driven loss of center of symmetry is similar to the type-II multiferroics. The discovery of 5d oxides $\text{Pb}_2\text{NiOsO}_6$ together with $\text{Pb}_2\text{CoOsO}_6$ establishes a new class of noncentrosymmetric AFM metallic oxides.

■ ASSOCIATED CONTENT

Supporting Information

The Supporting Information is available free of charge at <https://pubs.acs.org/doi/10.1021/acs.chemmater.1c01032>.

Refined room-temperature SXRD pattern and the corresponding crystal structure information, refined PND data at 98 and 1.5 K and the corresponding crystal structure information, evolution of nuclear and magnetic structures with temperature for $\text{Pb}_2\text{NiOsO}_6$ from sequential refinements using NPD data, and DFT calculations of $\text{Pb}_2\text{NiOsO}_6$ with different magnetic states (PDF)

■ AUTHOR INFORMATION

Corresponding Authors

Emma E. McCabe – School of Physical Sciences, University of Kent, Canterbury, Kent CT2 7NH, U.K.; Department of Physics, Durham University, Durham DH1 3LE, U.K.;
ORCID.org/0000-0001-5868-4570;
Email: emma.mccabe@durham.ac.uk

Martha Greenblatt – Department of Chemistry and Chemical Biology, Rutgers, the State University of New Jersey, Piscataway, New Jersey 08854, United States; ORCID.org/0000-0002-1806-2766; Email: greenbla@chem.rutgers.edu

Authors

Hai L. Feng – Department of Chemistry and Chemical Biology, Rutgers, the State University of New Jersey, Piscataway, New Jersey 08854, United States; Beijing National Laboratory for Condensed Matter Physics and Institute of Physics, Chinese Academy of Sciences, Beijing 100190, China; ORCID.org/0000-0002-2699-3958

Chang-Jong Kang – Department of Physics and Astronomy, Rutgers, the State University of New Jersey, Piscataway, New Jersey 08854, United States; Department of Physics, Chungnam National University, Daejeon 34134, South Korea; ORCID.org/0000-0003-2895-4888

Pascal Manuel – ISIS Facility, STFC, Rutherford Appleton Laboratory, Didcot, Oxfordshire OX11 0QX, U.K.

Fabio Orlandi – ISIS Facility, STFC, Rutherford Appleton Laboratory, Didcot, Oxfordshire OX11 0QX, U.K.; ORCID.org/0000-0001-6333-521X

Yu Su – International Center for Materials Nanoarchitectonics (WPI-MANA), National Institute for Materials Science, Tsukuba, Ibaraki 305-0044, Japan; Graduate School of Chemical Sciences and Engineering, Hokkaido University, Sapporo, Hokkaido 060-0810, Japan

Jie Chen – International Center for Materials Nanoarchitectonics (WPI-MANA), National Institute for Materials Science, Tsukuba, Ibaraki 305-0044, Japan; Graduate School of Chemical Sciences and Engineering, Hokkaido University, Sapporo, Hokkaido 060-0810, Japan; ORCID.org/0000-0001-9609-669X

Yoshihiro Tsujimoto – International Center for Materials Nanoarchitectonics (WPI-MANA), National Institute for Materials Science, Tsukuba, Ibaraki 305-0044, Japan; Graduate School of Chemical Sciences and Engineering, Hokkaido University, Sapporo, Hokkaido 060-0810, Japan; ORCID.org/0000-0003-2140-3362

Joke Hadermann – EMAT, University of Antwerp, 2020 Antwerp, Belgium; ORCID.org/0000-0002-1756-2566

Gabriel Kotliar – Department of Physics and Astronomy, Rutgers, the State University of New Jersey, Piscataway, New Jersey 08854, United States

Kazunari Yamaura – International Center for Materials Nanoarchitectonics (WPI-MANA), National Institute for Materials Science, Tsukuba, Ibaraki 305-0044, Japan; Graduate School of Chemical Sciences and Engineering, Hokkaido University, Sapporo, Hokkaido 060-0810, Japan; ORCID.org/0000-0003-0390-8244

Complete contact information is available at:

<https://pubs.acs.org/10.1021/acs.chemmater.1c01032>

Author Contributions

^{††}H.L.F. and C.-J.K. contributed equally.

Notes

The authors declare no competing financial interest.

■ ACKNOWLEDGMENTS

C.-J.K., G.K., and M.G. were supported by the U.S. Department of Energy, Office of Science, Basic Energy Science

as a part of the Computational Materials Science Program through the Center for Computational Design of Functional Strongly Correlated Materials and Theoretical Spectroscopy under DOE grant no. DE-FOA-0001276. This study was supported in part by JSPS KAKENHI grant no. JP20H05276, a research grant from Nippon Sheet Glass Foundation for Materials Science and Engineering (grant no. 40-37), and Innovative Science and Technology Initiative for Security (grant no. JPJ004596) from Acquisition, Technology & Logistics Agency (ATLA), Japan. We are grateful to the ISIS Neutron and Muon Source (S.T.F.C., U.K.) for the provision of neutron diffraction beamtime.⁵⁴

■ REFERENCES

- (1) Goodenough, J. B. *Magnetism and the Chemical Bond*; Interscience Publisher, 1963; pp 165–275.
- (2) Komarek, A. C.; Streltsov, S. V.; Isobe, M.; Moller, T.; Hoelzel, M.; Senyshyn, A.; Trots, D.; Fernandez-Diaz, M. T.; Hansen, T.; Gotou, H.; Yagi, T.; Ueda, Y.; Anisimov, V. I.; Grueninger, M.; Khomskii, D. I.; Braden, M. CaCrO₃ An Anomalous Antiferromagnetic Metallic Oxide. *Phys. Rev. Lett.* **2008**, *101*, 167204.
- (3) Cava, R. J.; Batlogg, B.; Krajewski, J. J.; Gammel, P.; Poulsen, H. F.; Peck, W. F.; Rupp, L. W. Antiferromagnetism and Metallic Conductivity in Nb₁₂O₂₉. *Nature* **1991**, *350*, 598–600.
- (4) Cheng, J.-G.; Zhou, J.-S.; Goodenough, J. B.; Zhou, H. D.; Wiebe, C. R.; Takami, T.; Fujii, T. Spin Fluctuations in the Antiferromagnetic metal Nb₁₂O₂₉. *Phys. Rev. B: Condens. Matter Mater. Phys.* **2009**, *80*, 134428.
- (5) Argyriou, D. N.; Mitchell, J. F.; Radaelli, P. G.; Bordallo, H. N.; Cox, D. E.; Medarde, M.; Jorgensen, J. D. Lattice effects and magnetic structure in the layered colossal magnetoresistance manganite La₂–2xSr₁+2xMn₂O₇, x=0.3. *Phys. Rev. B: Condens. Matter Mater. Phys.* **1999**, *59*, 8695–8702.
- (6) Yoshida, Y.; Ikeda, S. I.; Matsuhashita, H.; Shirakawa, N.; Lee, C. H.; Katano, S. Crystal and Magnetic Structure of Ca₃Ru₂O₇. *Phys. Rev. B: Condens. Matter Mater. Phys.* **2005**, *72*, 054412.
- (7) Berlijn, T.; Snijders, P. C.; Delaire, O.; Zhou, H. D.; Maier, T. A.; Cao, H. B.; Chi, S. X.; Matsuda, M.; Wang, Y.; Koehler, M. R.; Kent, P. R. C.; Weitering, H. H. Itinerant Antiferromagnetism in RuO₂. *Phys. Rev. Lett.* **2017**, *118*, 077201.
- (8) Zhu, Z. H.; Strempfer, J.; Rao, R. R.; Occhialini, C. A.; Pelliciari, J.; Choi, Y.; Kawaguchi, T.; You, H.; Mitchell, J. F.; Shao-Horn, Y.; Comin, R. Anomalous Antiferromagnetism in Metallic RuO₂ Determined by Resonant X-Ray Scattering. *Phys. Rev. Lett.* **2019**, *122*, 017202.
- (9) Guo, H.; Li, Z. W.; Zhao, L.; Hu, Z.; Chang, C. F.; Kuo, C. Y.; Schmidt, W.; Piovano, A.; Pi, T. W.; Sobolev, O.; Khomskii, D. I.; Tjeng, L. H.; Komarek, A. C. Antiferromagnetic Correlations in the Metallic Strongly Correlated Transition Metal Oxide LaNiO₃. *Nat. Commun.* **2018**, *9*, 43.
- (10) Witczak-Krempa, W.; Chen, G.; Kim, Y. B.; Balents, L. Correlated Quantum Phenomena in the Strong Spin-Orbit Regime. *Annu. Rev. Condens. Matter Phys.* **2014**, *5*, 57–82.
- (11) Jacobsen, H.; Feng, H. L.; Princep, A. J.; Rahn, M. C.; Guo, Y.; Chen, J.; Matsuhashita, Y.; Tsujimoto, Y.; Nagao, M.; Khalayav, D.; Manuel, P.; Murray, C. A.; Donnerer, C.; Vale, J. G.; Sala, M. M.; Yamaura, K.; Boothroyd, A. T. Magnetically Induced Metal-Insulator Transition in Pb₂CaOsO₆. *Phys. Rev. B* **2020**, *102*, 214409.
- (12) Mandrus, D.; Thompson, J. R.; Gaal, R.; Forro, L.; Brayan, J. C.; Chakoumakos, B. C.; Woods, L. M.; Sales, B. C.; Fishman, R. S.; Keppns, V. Continuous Metal-Insulator Transition in the Pyrochlore Cd₂Os₂O₇. *Phys. Rev. B: Condens. Matter Mater. Phys.* **2001**, *63*, 195104.
- (13) Padilla, W. J.; Mandrus, D.; Basov, D. N. Searching for the Slater Transition in the Pyrochlore Cd₂Os₂O₇ with Infrared Spectroscopy. *Phys. Rev. B: Condens. Matter Mater. Phys.* **2005**, *66*, 035120.
- (14) Calder, S.; Garlea, V. O.; McMorrow, D. F.; Lumsden, M. D.; Stone, M. B.; Lang, J. C.; Kim, J.-W.; Schueter, J. A.; Shi, Y. G.; Yamaura, K.; Sun, Y. S.; Tsujimoto, Y.; Christianson, A. D. Magnetically Driven Metal-Insulator Transition in NaOsO₃. *Phys. Rev. Lett.* **2012**, *108*, 257209.
- (15) Shi, Y.; Guo, Y.; Wang, X.; Princep, A. J.; Khalayav, D.; Manuel, P.; Michiue, Y.; Sato, A.; Tsuda, K.; Yu, S.; Arai, M.; Shirako, Y.; Akaogi, M.; Wang, N.; Yamaura, K.; Boothroyd, A. T. A Ferroelectric-like Structural Transition in a Metal. *Nat. Mater.* **2013**, *12*, 1024–1027.
- (16) Princep, A. J.; Feng, H. L.; Guo, Y. F.; Lang, F.; Weng, H. M.; Manuel, P.; Khalayav, D.; Senyshyn, A.; Rahn, M. C.; Yuan, Y. H.; Matsuhashita, Y.; Blundell, S. J.; Yamaura, K.; Boothroyd, A. T. Magnetically Driven Loss of Centrosymmetry in Metallic Pb₂CoOsO₆. *Phys. Rev. B* **2020**, *102*, 104410.
- (17) Jiao, Y.; Fang, Y.-W.; Sun, J.; Shan, P.; Yu, Z.; Feng, H. L.; Wang, B.; Ma, H.; Uwatoko, Y.; Yamaura, K.; Guo, Y.; Chen, H.; Cheng, J. Coupled Magnetic and Structural Phase Transitions in the Antiferromagnetic Polar Metal Pb₂CoOsO₆ Under Pressure. *Phys. Rev. B* **2020**, *102*, 144418.
- (18) Yamaura, K. Short Review of High-Pressure Crystal Growth and Magnetic and Electrical Properties of Solid-State Osmium Oxides. *J. Solid State Chem.* **2016**, *236*, 45–54.
- (19) Tanaka, M.; Katsuya, Y.; Matsuhashita, Y.; Sakata, O. Development of a Synchrotron Powder Diffractometer with a One-Dimensional X-Ray Detector for Analysis of Advanced Materials. *J. Ceram. Soc. Jpn.* **2013**, *121*, 287–290.
- (20) Tanaka, M.; Katsuya, Y.; Yamamoto, A. A New Large Radius Imaging Plate Camera for High-Resolution and High-Throughput Synchrotron X-Ray Powder Diffraction by Multiexposure Method. *Rev. Sci. Instrum.* **2008**, *79*, 075106.
- (21) Izumi, F.; Ikeda, T. A Rietveld-Analysis Programm RIETAN-98 and its Applications to Zeolites. *Mater. Sci. Forum* **2000**, *321–324*, 198–205.
- (22) Momma, K.; Izumi, F. VESTA 3 for Three-Dimensional Visualization of Crystal, Volumetric and Morphology data. *J. Appl. Crystallogr.* **2011**, *44*, 1272–1276.
- (23) Chapon, L. C.; Manuel, P.; Radaelli, P. G.; Benson, C.; Perrott, L.; Ansell, S.; Rhodes, N. J.; Raspino, D.; Duxbury, D.; Spill, E.; Norris, J. Wish: The New Powder and Single Crystal Magnetic Diffractometer on the Second Target Station. *Neutron News* **2011**, *22*, 22–25.
- (24) Coelho, A. A. Indexing of Powder Diffraction Patterns by Iterative Use of Singular Value Decomposition. *J. Appl. Crystallogr.* **2003**, *36*, 86–95.
- (25) Coelho, A. A. *Topas Academic: General Profile and Structure Analysis Software for Powder Diffraction Data*; Bruker AXS: Karlsruhe, Germany, 2012.
- (26) Campbell, B. J.; Stokes, H. T.; Tanner, D. E.; Hatch, D. M. ISODISPLACE: a web-based tool for exploring structural distortions. *J. Appl. Crystallogr.* **2006**, *39*, 607–614.
- (27) Blaha, P.; Schwarz, K.; Madsen, G. K. H.; Kvasnicka, D.; Luitz, J. *WIEN2K, an Augmented Plane Wave + Local Orbitals Program for Calculating Crystal Properties*; Technische Universität Wien: Wien, Austria, 2001.
- (28) Perdew, J. P.; Burke, K.; Ernzerhof, M. Generalized Gradient Approximation Made Simple. *Phys. Rev. Lett.* **1996**, *77*, 3865–3868.
- (29) Anisimov, V. I.; Solovyev, I. V.; Korotin, M. A.; Czyzyk, M. T.; Sawatzky, G. A. Density-Functional Theory and Ni Photoemission Spectra. *Phys. Rev. B: Condens. Matter Mater. Phys.* **1993**, *48*, 16929–16934.
- (30) Anisimov, V. I.; Aryasetiawan, F.; Lichtenstein, A. I. First-Principles Calculations of the Electronic Structure and Spectra of Strongly Correlated Systems: The LDA+U Method. *J. Phys.: Condens. Matter* **1997**, *9*, 767–808.
- (31) Morrow, R.; Samanta, K.; Dasgupta, T. S.; Xiong, J.; Freeland, J. W.; Haskel, D.; Woodward, P. M. Magnetism in Ca₂CoOsO₆ and Ca₂NiOsO₆: Unraveling the Mystery of Superexchange Interactions between 3d and 5d Ions. *Chem. Mater.* **2016**, *28*, 3666–3675.

(32) Ramesha, K.; Sebastian, L.; Eichhorn, B.; Gopalakrishnan, J. Perovskite and Pyrochlore Modifications of $\text{Pb}_2\text{MnReO}_6$: Synthesis, Structure, and Electronic Properties. *Chem. Mater.* **2003**, *15*, 668–674.

(33) Ivanov, S. A.; Nordblad, P.; Mathieu, R.; Tellgren, R.; Ritter, C. Structural and Magnetic Properties of the Ordered Perovskite $\text{Pb}_2\text{CoTeO}_6$. *Dalton Trans.* **2010**, *39*, 11136–11148.

(34) Brown, I. D.; Altermatt, D. Bond-valence parameters obtained from a systematic analysis of the Inorganic Crystal Structure Database. *Acta Crystallogr., Sect. B: Struct. Sci.* **1985**, *41*, 244–247.

(35) Bresc, N. E.; O'Keeffe, M. Bond-Valence Parameters for Solids. *Acta Crystallogr., Sect. B: Struct. Sci.* **1991**, *47*, 192–197.

(36) Macquart, R.; Kim, S.-J.; Gemmill, W. R.; Stalick, J. K.; Lee, Y.; Vogt, T.; zur Loyer, H.-C. Synthesis, Structure, and Magnetic Properties of $\text{Sr}_2\text{NiOsO}_6$ and $\text{Ca}_2\text{NiOsO}_6$: Two New Osmium-Containing Double Perovskites. *Inorg. Chem.* **2005**, *44*, 9676–9683.

(37) Feng, H. L.; Calder, S.; Ghimire, M. P.; Yuan, Y. H.; Shirako, Y.; Tsujimoto, Y.; Matsushita, Y.; Hu, Z. W.; Kuo, C. Y.; Tjeng, L. H.; Pi, T. W.; Soo, Y. L.; He, J. F.; Tanaka, M.; Katsuya, Y.; Richter, M.; Yamaura, K. $\text{Ba}_2\text{NiOsO}_6$: A Dirac-Mott Insulator with Ferromagnetism Near 100 K. *Phys. Rev. B* **2016**, *94*, 235158.

(38) Yi, W.; Princep, A. J.; Guo, Y.; Johnson, R. D.; Khalyavin, D.; Manuel, P.; Senyshyn, A.; Presniakov, I. A.; Sobolev, A. V.; Matsushita, Y.; Tanaka, M.; Belik, A. A.; Boothroyd, A. T. $\text{Sc}_2\text{NiMnO}_6$: a Double Perovskite with Magnetoelectric Response Driven by Multiple Magnetic Orders. *Inorg. Chem.* **2015**, *54*, 8012–8021.

(39) Morrow, R.; Yan, J.; McGuire, M. A.; Freeland, J. W.; Haskel, D.; Woodward, P. M. Effects of Chemical Pressure on the Magnetic Ground States of the Osmate Double Perovskites SrCaCoOsO_6 and $\text{Ca}_2\text{CoOsO}_6$. *Phys. Rev. B: Condens. Matter Mater. Phys.* **2015**, *92*, 094435.

(40) Morrow, R.; Freeland, J. W.; Woodward, P. M. Probing the Links between Structure and Magnetism in $\text{Sr}_{2-x}\text{Ca}_x\text{FeOsO}_6$ Double Perovskites. *Inorg. Chem.* **2014**, *53*, 7983–7992.

(41) Tuxworth, A. J.; McCabe, E. E.; Free, D. G.; Clark, S. J.; Evans, J. S. O. Structural Characterization and Physical Properties of the New Transition Metal Oxselenide $\text{La}_2\text{O}_2\text{ZnSe}_2$. *Inorg. Chem.* **2013**, *52*, 2078–2085.

(42) McCabe, E. E.; Stock, C.; Rodrigues, E. E.; Wills, A. S.; Taylor, J. W.; Evans, J. S. O. Weak Spin Interactions in Mott Insulating $\text{La}_2\text{O}_2\text{Fe}_2\text{OSe}_2$. *Phys. Rev. B: Condens. Matter Mater. Phys.* **2014**, *89*, No. 100402(R).

(43) Taylor, A. E.; Morrow, R.; Lumsden, M. D.; Calder, S.; Upton, M. H.; Kolesnikov, A. I.; Stone, M. B.; Fishman, R. S.; Paramakanti, A.; Woodward, P. M.; Christianson, A. D. Origin of Magnetic Excitation Gap in Double Perovskite $\text{Sr}_2\text{FeOsO}_6$. *Phys. Rev. B* **2018**, *98*, 214422.

(44) Khalyavin, D. D.; Salak, A. N.; Olekhovich, N. M.; Pushkarev, A. V.; Radyush, Y. V.; Manuel, P.; Raevski, I. P.; Zheludkevich, M. L.; Ferreira, M. G. S. Polar and Antipolar Polymorphs of Metastable Perovskite $\text{BiFe}_{0.5}\text{Sc}_{0.5}\text{O}_3$. *Phys. Rev. B: Condens. Matter Mater. Phys.* **2014**, *89*, 174414.

(45) Prosandeev, S. A.; Khalyavin, D. D.; Raevski, I. P.; Salak, A. N.; Olekhovich, N. M.; Pushkarev, A. V.; Radyush, Y. V. Complex Antipolar $2\times 4\times 22$ Structure with Pnma Symmetry in BiFeO_3 and $\text{BiFe}_{1/2}\text{Sc}_{1/2}\text{O}_3$: First-Principles Calculations. *Phys. Rev. B: Condens. Matter Mater. Phys.* **2014**, *90*, 054110.

(46) Schoop, L. M.; Topp, A.; Lippmann, J.; Orlandi, F.; Müchler, L.; Vergniory, M. G.; Sun, Y.; Rost, A. W.; Duppel, V.; Krivenkov, M.; Sheoran, S.; Manuel, P.; Varykhalov, A.; Yan, B.; Kremer, R. K.; Ast, C. R.; Lotsch, B. V. Tunable Weyl and Dirac States in the Nonsymmorphic Compound CeSbTe . *Sci. Adv.* **2018**, *4*, No. eaar2317.

(47) Shannon, R. D. Revised Effective Ionic Radii and Systematic Studies of Interatomic Distances in Halides and Chalcogenides. *Acta Crystallogr., Sect. A: Cryst. Phys., Diffr., Theor. Gen. Crystallogr.* **1976**, *32*, 751–767.

(48) Walsh, A.; Payne, D. J.; Egddell, R. G.; Watson, G. W. Stereochemistry of Post-Transition Metal Oxides: Revision of the Classical Lone Pair Model. *Chem. Soc. Rev.* **2011**, *40*, 4455–4463.

(49) Tian, C.; Wibowo, A. C.; zur Loyer, H.-C.; Whangbo, M.-H. On the Magnetic Insulating States, Spin Frustration, and Dominant Spin Exchange of the Ordered Double-Perovskites $\text{Sr}_2\text{CuOsO}_6$ and $\text{Sr}_2\text{NiOsO}_6$: Density Functional Analysis. *Inorg. Chem.* **2011**, *50*, 4142–4148.

(50) Perez-Mato, J. M.; Gallego, S. V.; Elcoro, L.; Tasci, E.; Aroyo, M. I. Symmetry Conditions for Type II Multiferroicity in Commensurate Magnetic Structures. *J. Phys.: Condens. Matter* **2016**, *28*, 286001.

(51) Choi, Y. J.; Yi, H. T.; Lee, S.; Huang, Q.; Kiryukhin, V.; Cheong, S.-W. Ferroelectricity in an Ising Chain Magnet. *Phys. Rev. Lett.* **2008**, *100*, 047601.

(52) Shaikh, M.; Fathima, A.; Swamynadhan, M. J.; Das, H.; Ghosh, S. Investigation into Cation-Ordered Magnetic Polar Double Perovskite Oxides. *Chem. Mater.* **2021**, *33*, 1594–1606.

(53) Ghimire, M. P.; Hu, X. Compensated Half Metallicity in Osmium Double Perovskite Driven by Doping Effects. *Mater. Res. Express* **2016**, *3*, 106107.

(54) McCabe, E.; Tan, X.; Li, M.-R.; Yamaura; Orlandi, F.; Manuel, P.; Greenblatt, M.; Cascos Jimenez, V. A. Magnetism and electronic structure of 3d 5d double perovskites. *STFC ISIS Neutron and Muon Source*, 2018, DOI: 10.5286/ISIS.E.RB1820111.